

# Soliton frequency comb at microwave rates in a high-Q silica microresonator

XU YI,<sup>†</sup> QI-FAN YANG,<sup>†</sup> KI YOUL YANG,<sup>†</sup> MYOUNG-GYUN SUH, AND KERRY VAHALA<sup>\*</sup>

*T. J. Watson Laboratory of Applied Physics, California Institute of Technology, Pasadena, California 91125, USA*

*<sup>\*</sup>Corresponding author: vahala@caltech.edu*

*Received 23 September 2015; revised 28 October 2015; accepted 17 November 2015 (Doc. ID 250710); published 17 December 2015*

Frequency combs are having a broad impact on science and technology because they provide a way to coherently link radio/microwave-rate electrical signals with optical-rate signals derived from lasers and atomic transitions. Integrating these systems on a photonic chip would revolutionize instrumentation, time keeping, spectroscopy, navigation, and potentially create new mass-market applications. A key element of such a system-on-a-chip will be a mode-locked comb that can be self-referenced. The recent demonstration of soliton mode locking in crystalline and silicon nitride microresonators has provided a way to both mode lock and generate femtosecond time-scale pulses. Here, soliton mode locking is demonstrated in high-Q silica resonators. The resonators produce low-phase-noise soliton pulse trains at readily detectable pulse rates—two essential properties for the operation of frequency combs. A method for the long-term stabilization of the solitons is also demonstrated, and is used to test the theoretical dependence of the comb power, efficiency, and soliton existence power on the pulse width. The influence of the Raman process on the soliton existence power and efficiency is also observed. The resonators are microfabricated on silicon chips and feature reproducible modal properties required for soliton formation. A low-noise and detectable pulse rate soliton frequency comb on a chip is a significant step towards a fully integrated frequency comb system. © 2015 Optical Society of America

**OCIS codes:** (140.3460) Lasers; (190.4360) Nonlinear optics, devices; (140.3945) Microcavities; (140.7090) Ultrafast lasers.

<http://dx.doi.org/10.1364/OPTICA.2.001078>

## 1. INTRODUCTION

The optical frequency comb is revolutionizing a wide range of subjects spanning spectroscopy to time standards [1–9]. Since their invention, a miniaturized approach to the formation of a comb of optical frequencies has been proposed in high-Q microresonators [10,11]. These microcombs, or Kerr combs, have been demonstrated in several material systems [12–15], including certain planar systems suitable for monolithic integration [16–20]. They have been applied in demonstrations of microwave generation [12], waveform synthesis [18], optical atomic clocks [21] and coherent communications [22]. Microcombs were initially realized through a process of cascaded four-wave mixing [10] driven by parametric oscillation [23,24]. However, a recent advance has been the demonstration of mode locking through the formation of dissipative Kerr solitons in microresonators [25,26]. While the initial work on microcombs demonstrated phase-locked states [19,27–30], including pulse generation [31], solitons are both phase locked and, being pulses, can be readily broadened spectrally [25]. Moreover, resonator dispersion can be engineered so as to create coherent dispersive waves that broaden the soliton comb spectrum within the resonator [26,32]. Both of these features can simplify the comb self-referencing process. Finally, solitons have a very predictable spectral envelope, which is useful in any application where individual comb teeth are

accessed for measurement. Dissipative Kerr solitons balance dispersion with the Kerr nonlinearity while also balancing optical loss with parametric gain from the Kerr nonlinearity [25,33]. They have been observed in fiber resonator systems [34]. In microresonators, these solitons have been observed in crystalline [25,35,36] and in silicon nitride-based systems [26]. Crystalline system solitons have also been externally broadened to 2/3 of an octave, enabling the detection of the comb offset frequency [37].

In a self-referenced frequency comb, the optical frequency  $\omega_m$  of the  $m$ th comb tooth can be written as a simple function of two frequencies, the pulse repetition frequency  $\omega_r$  and the offset frequency  $\omega_{\text{offset}}$  such that  $\omega_m = m\omega_r + \omega_{\text{offset}}$ . To achieve self-referenced operation, these frequencies must be detectable and ideally occur at rates for which low-noise electronics is available. In this work, a comb of frequencies is generated by soliton mode locking in a silica resonator. The soliton pulse trains occur at a repetition frequency that is both readily detectable with commercial photo detectors and that enables the use of low-noise electronics. Moreover, the free-running phase noise of the detected pulse train is comparable to a good K-band signal source. Aside from the first observation of soliton frequency combs in a silica microresonator, the control of soliton properties through a novel locking technique is demonstrated. This technique is used to controllably explore the soliton regime of operation, including

measuring the soliton efficiency and existence power, as well as measuring the soliton power and power per line versus the soliton pulse width for comparison with the theoretical values. Servo locking also enables stable mode locking indefinitely, as well as operation at optimal detuning with respect to the comb pumping efficiency. The influence of the Raman process on the soliton is also observed. In addition to Raman-induced self-shifting of the soliton spectrum [38], the soliton existence power and efficiency are observed to be influenced by Raman interactions at short pulse durations. Finally, the silica resonator used here is fabricated on a silicon chip, which enables reproducible avoided-mode-crossing control through the micro-lithographic control of the resonator geometry.

## 2. RESONATOR CHARACTERIZATION

The silica wedge resonators were fabricated using float-zone silicon wafers [39]. The devices exhibit a nearly constant finesse over a wide range of diameters and have previously been applied for comb generation at free spectral range (FSR) values from 2.6 to 220 GHz, including the formation of stable phase-locked comb states [19,21]. In the present work, 3 mm diameter devices with an FSR of 22 GHz were prepared, and intrinsic  $Q$ -factors were characterized by the linewidth measurement to lie near 400 million. To both characterize the soliton tuning range (see discussion below) and to provide a separate test of the  $Q$ -factor, the threshold for parametric oscillation was measured and compared to the theoretical value [19,23]:

$$P_{\text{th}} = \frac{\pi n \omega_o A_{\text{eff}}}{4 \eta n_2} \frac{1}{D_1 Q^2}, \quad (1)$$

where  $A_{\text{eff}} \sim 60 \mu\text{m}^2$  is the effective mode area,  $n$  is the refractive index,  $n_2$  is the Kerr coefficient,  $D_1$  is the FSR in rad/s units,  $\eta = Q/Q_{\text{ext}}$  characterizes the waveguide to resonator loading, where  $Q_{\text{ext}}$  is the external or coupling  $Q$ -factor and  $Q$  is the total  $Q$ -factor (intrinsic loss and loading included), and  $\omega_o$  is the optical frequency. A schematic of the experimental characterization setup is provided in Fig. 1(a). The typical measured threshold powers were around 2.5 mW and were consistent with the measured  $Q$ -factors.

The mode family that is phase locked to form the soliton pulse train must feature anomalous dispersion [23] and also minimal distortion of the dispersion caused by other mode families within the resonator [40]. The first of these requirements is straightforward in silica wedge resonators when operated in the 1.5  $\mu\text{m}$  band [41]. However, the second requirement is more complicated, as wedge resonators feature many transverse mode families. Minimizing avoided-crossing behavior is achieved by screening wedge disks to find combinations of diameter, thickness, and wedge angle that produce avoided-crossing free spectral regions. In addition, it is observed that high- $Q$ -factor mode families are generally more immune to avoided-crossing distortion. To characterize both mode family dispersion and avoided-mode-crossing behavior, the mode frequencies were measured using a tunable laser that was calibrated with a fiber Mach–Zehnder interferometer. A measurement taken on a typical mode family used to produce solitons is presented in Fig. 1(b). A parabolic fit to the data featuring an anomalous dispersion of 17 kHz/FSR is provided for comparison to the data. Two avoided mode crossings are apparent in the spectrum. Numerical simulation of the resonator dispersion allowed the identification of the mode families believed to be responsible for the avoided mode crossing.

Generally, the dispersion modeling was found to be in excellent agreement with measured dispersion curves for the soliton mode family and these other mode families.

## 3. MEASUREMENT OF COMB PROPERTIES

Modes belonging to families featuring both anomalous dispersion and well-behaved spectra (i.e., few avoided crossings) were pumped using a scanning fiber laser. Solitons form when the pump frequency is red detuned relative to an optical mode, and give rise to characteristic steps in the pump power transmission versus tuning [25]. As has been described elsewhere, the excitation of stable soliton trains is complicated by the thermal non-linearity of the resonator [26], which is well known to destabilize a red-detuned pump wave [42]. Fortunately, solitons feature power dependence with the tuning of the pump wave that reverses this behavior and that will stabilize the pump on the red side of the resonance once the nonsoliton transients have died away. To induce stability, the two-step protocol was employed [26]. Both single and multiple soliton states were stably excited in different resonators. Figure 1(c) shows the spectrum measured for a single-soliton state. The square of a hyperbolic secant function is also overlaid onto the spectrum to verify the characteristic single-soliton spectral shape. From this fitting, the soliton pulse width  $\tau$  is inferred to be 130 fs where the pulse shape is  $\text{sech}^2(t/\tau)$ . (Note: this definition of pulse width is  $0.57\times$  the FWHM width of the soliton pulse). The presence of small spurs in the spectrum of Fig. 1(c) correlate with the appearance of avoided crossings in the mode dispersion spectrum in Fig. 1(b).

Direct confirmation of single-soliton generation is provided by frequency-resolved optical gating (FROG) and autocorrelation traces [see Fig. 1(d)]. In these measurements, the pump laser was suppressed by fiber Bragg-grating filters, and a dispersion compensation of -1.5 ps/nm was applied using a programmable optical filter before the comb was amplified by an erbium-doped fiber amplifier (EDFA). A pulse width of 250 fs with a pulse period of 46 ps is inferred from this data. The measured pulse width is larger than that fitted from the optical spectrum (130 fs) due to the limited wavelength bandwidth of the optical pre-amplifier used in this measurement. The FROG data was also used to reconstruct the phase of the spectrum and showed a constant phase across the comb lines.

An important feature of the soliton states generated in this work is their detectable and stable repetition rate. Figure 2(a) contains the phase noise spectra of the detected soliton fundamental repetition frequency measured using single solitons generated with three different resonators. The upper right inset of Fig. 2(a) is a typical radio frequency spectrum of the fundamental repetition frequency. The repetition frequency can be seen to be 21.92 GHz (resolution bandwidth is 10 kHz), and has an excellent stability that is comparable to a good K-band microwave oscillator. For example, one of the devices measured has a phase noise level of -100 dBc/Hz at a 10 kHz offset (referenced to a 10 GHz carrier frequency). We believe that some of the variations observable in these spectra are not fundamental, but instead are related to the pump laser noise. For example, the step feature in the spectrum near the 20 kHz offset frequency also appears in the frequency noise of the pump laser [see green curve in Fig. 2(a)].

The ability to reproduce mode family dispersion characteristics in different resonators was investigated. Figures 2(b) and 2(c) give

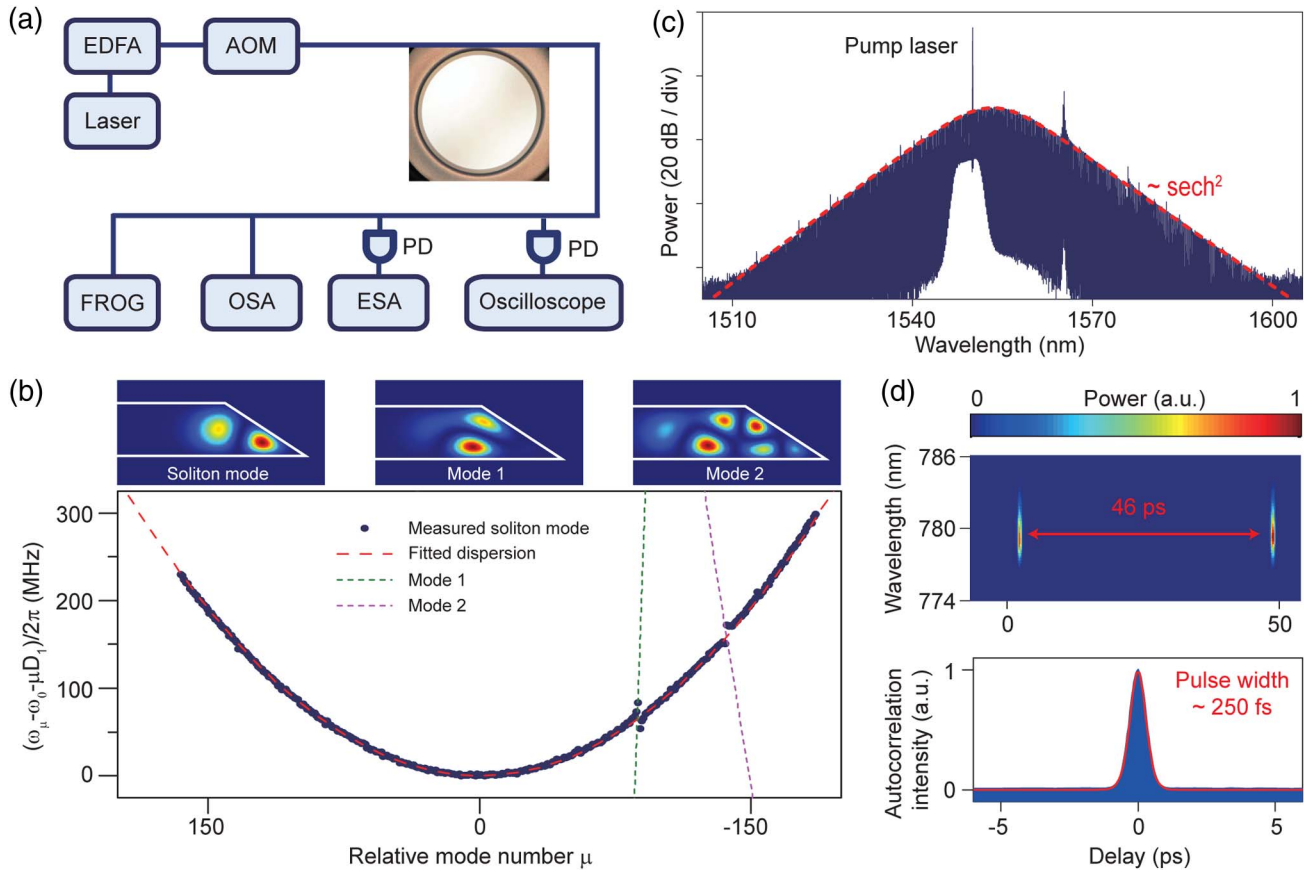


**Fig. 1.** Experimental setup, soliton mode family dispersion, optical spectrum, and autocorrelation. (a) Experimental setup. A continuous-wave fiber laser is amplified by an EDFA. The laser frequency is separately monitored using a fiber Mach–Zehnder interferometer (not shown). To implement the two-step protocol, the laser is modulated by an acousto-optic modulator (AOM). The laser is coupled to a high- $Q$  wedge resonator using a fiber taper. The power transmission and microwave beatnote are detected by photo detectors (PD) and sent to an oscilloscope and electrical spectrum analyzer (ESA). The soliton optical spectra are measured using an optical spectrum analyzer (OSA). Dispersion compensation (not shown) is employed before the solitons are amplified for autocorrelation and the FROG measurement. Polarization controllers, optical isolators, and optical Bragg-grating filters are not shown. (b) Measured frequency dispersion (blue points) belonging to the soliton-forming mode family is plotted versus the relative mode number,  $\mu$ . To construct this plot, the mode frequency relative to a  $\mu = 0$  mode (mode to be pumped) is measured using a calibrated Mach–Zehnder interferometer (fiber optic-based). To second order in the mode number, the mode frequency is given by the Taylor expansion,  $\omega_\mu = \omega_0 + \mu D_1 + \frac{1}{2} \mu^2 D_2$ , and the dashed red curve is a fit using  $D_1/2\pi = 21.92$  GHz and  $D_2/2\pi = 17$  kHz. In the plot, the mode frequencies are offset by the linear term in the Taylor expansion to make clear the second-order group dispersion. The measured modes span wavelengths from 1520 to 1580 nm, and  $\mu = 0$  corresponds to a wavelength close to 1550 nm. The presence of nonsoliton-forming mode families can be seen through the appearance of avoided mode crossings (spur-like features) that perturb the parabolic shape. Simulations of the nonsoliton mode families believed to be responsible for these spurs are provided (see mode 1 and mode 2 dashed curves). In addition, the normalized transverse intensity profiles for the soliton and nonsoliton spatial modes are provided at the top of the panel (red indicates higher mode intensity). The simulation used the Sellmeier equation for the refractive index of silica. The oxide thickness, wedge angle, and radius were finely adjusted to produce the indicated fits. (c) The optical spectrum of a single soliton state is shown with a  $\text{sech}^2$  envelope (red dashed line) superimposed for comparison. The pump laser is suppressed by 20 dB with an optical Bragg-grating filter. (d) FROG (upper) and autocorrelation trace (lower) of the soliton state in (c). The optical pulse period is 46 ps and the fitted pulse width is 250 fs (red solid line).

the results of mode family dispersion measurements and soliton optical spectra on two resonators that are close in size and shape to the device in Fig. 1. There is high level of consistency in both the magnitude of the dispersion and also the minimal presence of mode crossings in the measured spectra. This level of consistency was sufficient across many devices to provide the ready observation of soliton steps. Nonetheless, there are observable variations in the nature of the soliton steps formed in scanning the resonators. The corresponding soliton steps under the pump frequency scan are shown in Fig. 2(d). Also, the microwave phase noise spectra in Fig. 2(a) were measured on soliton trains using these same three devices, and exhibit slight differences.

#### 4. PUMP-RESONATOR DETUNING LOCK

For steady-state soliton generation, it was possible to pump the resonator without any frequency locking control of the pump laser (i.e., open loop). In this mode of operation, solitons were generated for several hours provided that the pump power was high (see comment in next section). However, several soliton properties depend upon the pump-resonator detuning,  $\delta\omega \equiv \omega_o - \omega_p$ , where  $\omega_o$  is the resonator frequency and  $\omega_p$  is the pump frequency. It is therefore desirable to stabilize the detuning of the pump relative to the cavity. For example, the soliton power and pulse width are given by the following expressions [25,43,44]:



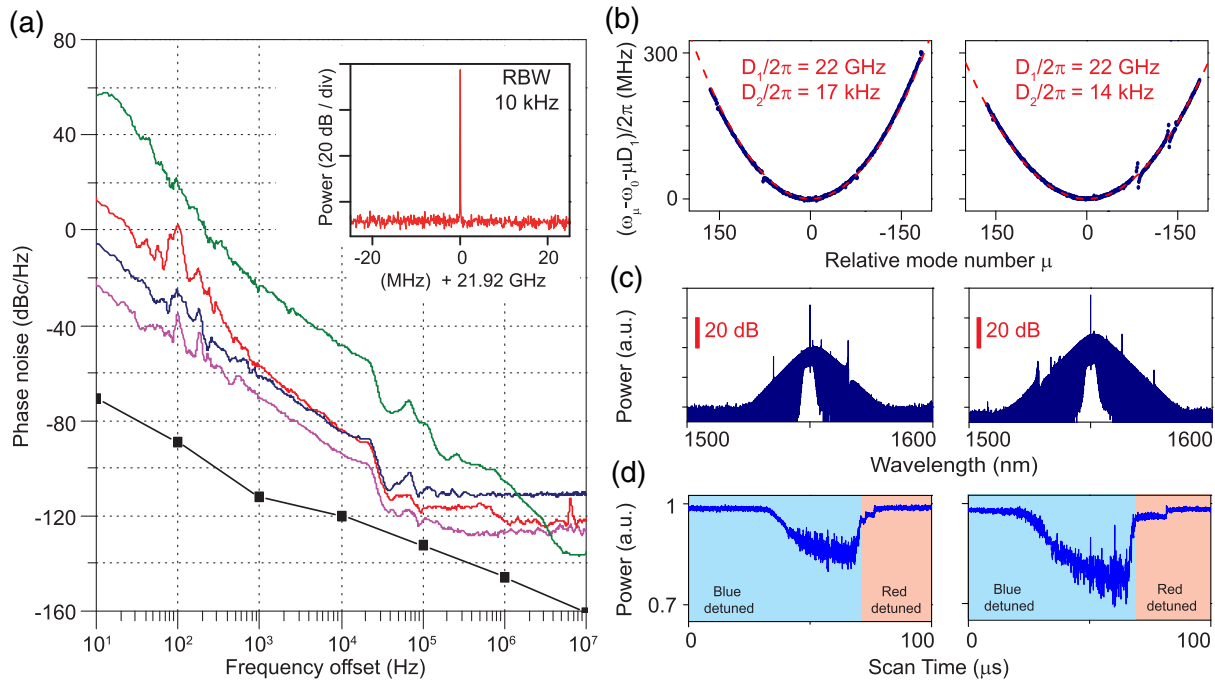


**Fig. 2.** Detected phase noise and electrical spectra for three devices with corresponding mode dispersion and soliton data. (a) Phase noise spectral density function plotted versus offset frequency from the detected soliton repetition frequency of three different devices. A Rohde & Schwarz phase noise analyzer was used in the measurement. Inset shows the electrical spectrum of the soliton repetition frequency (21.92 GHz) for one device. The other devices had similar spectra, with repetition frequencies of 22.01 and 21.92 GHz. The phase noise of the fiber pump laser is shown in green and was generated by mixing two nominally identical pump lasers to create a 2.7 GHz electrical beatnote. Several features in the pump laser phase noise are reproduced in the soliton phase noise (see features near and above 20 kHz). The black line connecting the square dots is the measurement floor of the phase noise analyzer. (b),(c) The mode dispersion spectra and soliton optical spectra are presented for two of the devices measured in (a). The third device in (a) is from Fig. 1. (d) Pump power transmission is plotted versus tuning across a resonance used to generate the soliton spectra in (c). The data show the formation of steps as the pump tunes red relative to the resonance. Both the blue-detuned and the red-detuned operation of the pump relative to the resonance are inferred from generation of an error signal using a Pound–Drever–Hall system-operated open loop.

$$P_{\text{sol}} = \frac{2\eta A_{\text{eff}}}{n_2 Q} \sqrt{-2nc\beta_2 \delta\omega}, \quad (2)$$

$$\tau = \sqrt{-\frac{c\beta_2}{2n\delta\omega}}, \quad (3)$$

where  $\beta_2 = -nD_2/cD_1^2$  is the group velocity dispersion and is negative for anomalous dispersion. Because the amount of detuning,  $\delta\omega$ , will typically exceed tens of cavity linewidths, it is not immediately clear how standard locking methods can be applied. Moreover, such techniques may interfere with the mode-locking process itself. The technique demonstrated here uses the theoretical dependence of the average soliton comb power on the pump-resonator detuning [Eq. (2)]. This dependence means that  $\delta\omega$  can be servo locked by requiring the comb power to hold a fixed set point. Indeed, the implementation of this locking method is a test of the theoretical independence of the comb power and the pump power. The servo control also has the effect of fixing the soliton pulse width [see Eq. (3)].

To demonstrate the servo control method and to also test our theoretical predictions, several soliton properties were measured. The comb power and the maximum power per comb line were measured at a series of detuning values,  $\delta\omega/2\pi$ , estimated to range from 12.8 MHz ( $\tau = 187$  fs) to 29.6 MHz ( $\tau = 123$  fs), or approximately 13 to 30 cavity linewidths. At each point, the soliton spectrum was also recorded, which enables the calculation of the soliton pulse width  $\tau$ . The results of these measurements are

compiled in Fig. 3(a). Also, Fig. 3(b) shows the soliton spectrum measured at the detuning limits presented in Fig. 3(a). The dashed lines in Fig. 3(a) give the predicted comb power and maximum comb line power based on the following expressions for the comb power and the comb power spectral envelope [25,43,44]:

$$P_{\text{sol}} = -\frac{2c\eta A_{\text{eff}}\beta_2}{n_2 Q} \frac{1}{\tau}, \quad (4)$$

$$P(\Delta\omega) = -\frac{\pi c \eta A_{\text{eff}} \beta_2 D_1}{2 n_2 Q} \text{sech}^2\left(\frac{\pi \tau}{2} \Delta\omega\right), \quad (5)$$

where Eq. (4) is obtained by eliminating  $\delta\omega$  in Eqs. (2) and (3), and  $\Delta\omega$  denotes the comb tooth frequency relative to the comb's center frequency. Note that the peak power of the spectral envelope (i.e., the maximum comb tooth power) is determined entirely by the cavity properties. This feature is apparent in both the data in Fig. 3(a) and the spectra in Fig. 3(b). As an aside, Eqs. (2) and (3) are derived under an assumption of large frequency detuning in units of cavity linewidth, which is satisfactory for the current measurements.

An important benefit of the feedback control presented here is that it provides a convenient way to stabilize the mode-locked system indefinitely. For example, the system was operated continuously for over 24 h. For over 19 h of this period, comb properties were recorded and are presented in Fig. 4.

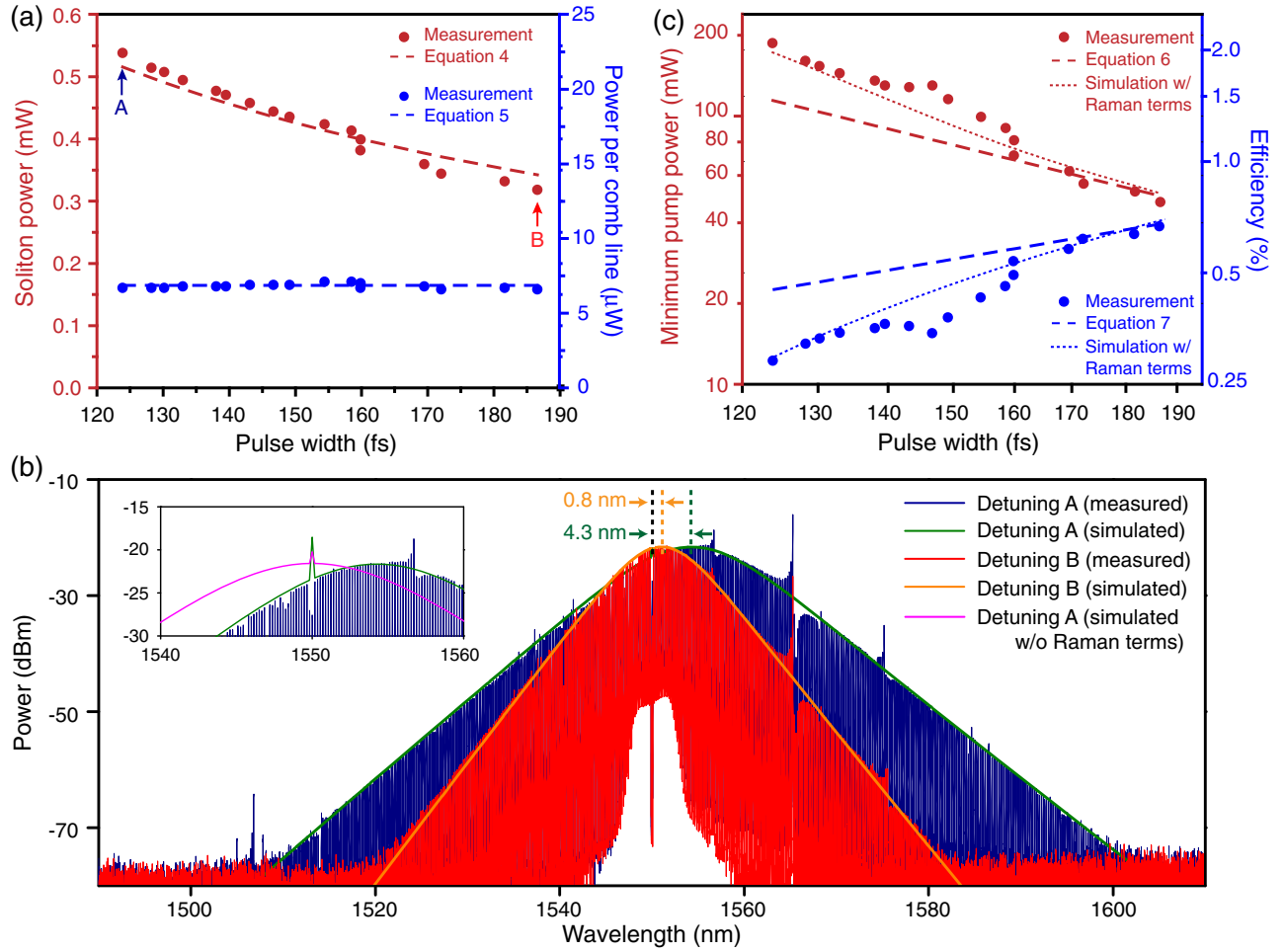


**Fig. 3.** Control of soliton properties. (a) Measured soliton comb output power is plotted versus measured soliton pulse width (red points) with comparison to Eq. (4) (dashed red line). The measured power per central comb line is plotted versus pulse width (blue points) with comparison to Eq. (5) (dashed blue line). (b) The observed soliton spectra at the limits of the measurement in Fig. 3(a) are shown [see arrows A and B in Fig. 3(a)]. Solid orange and green curves are simulations using the Lugiato–Lefever equation, which includes Raman terms. The indicated wavelength shifts between the pump and the centroid of the soliton spectrum result from Raman interactions with the soliton. The location of the pump line for both spectra is indicated by the dashed black line and has been suppressed by filtering. The inset shows a magnified view near the central region of the blue spectrum. The green (purple) envelope provides the Lugiato–Lefever simulation with (without) Raman terms. The green spike is the location of the pump. (c) The measured minimum pump power for soliton existence is plotted versus the measured soliton pulse width (red points) with comparison to Eq. (6) (dashed red line). The measured efficiency is plotted versus the measured soliton pulse width (blue points) with comparison to Eq. (7) (dashed blue line). The simulation using the Lugiato–Lefever equation including Raman terms improves the agreement with data (small dashed red and blue lines).

## 5. EXISTENCE POWER AND RAMAN

In units of cavity linewidth, the predicted maximum detuning for soliton existence is given by  $\delta\omega_{\max} \equiv \pi^2 P_{\text{in}} / 16 P_{\text{th}}$  [25,43,44]. This power dependence explains why increased pump power is effective in providing a stable, nonlocked soliton operation. At higher pumping powers, the solitons can survive over a wider range of tuning values, as the pump laser frequency drifts relative to the cavity resonant frequency. However, as noted above, it is preferable to prevent this relative drift. In addition to the reasons mentioned in the previous section, locking the detuning frequency,  $\delta\omega$ , enables operation at a lower (and hence more efficient) pump power setting that is close to the existence power limit for solitons of the desired pulse width.

To measure the minimum existence power,  $\delta\omega$  was held constant while the pump power was reduced until the soliton pulse train disappeared. Both the power level and the soliton spectrum

were recorded near the point of disappearance.  $\delta\omega$  was then reset to a new value, and the measurement was repeated. Figure 3(c) gives the minimum power measured this way plotted versus the pulse width (as calculated earlier from the soliton spectrum). Substituting for  $\delta\omega$  in Eq. (3) using  $\delta\omega_{\max}$  gives the following expression for the minimum pump power for soliton existence as a function of the pulse width [25,43,44]:

$$P_{\text{in}}^{\min} = -\frac{2c A_{\text{eff}} \beta_2}{\pi \eta n_2 \tau^2} \frac{1}{Q D_1}. \quad (6)$$

This expression is plotted in Fig. 3(c) (dashed red line). A deviation from the predicted dependence is observed. Improved agreement with the data is provided by a simulation (small dashed red line) using the Lugiato–Lefever equation (LLE) [25,44–47] augmented by Raman terms [48,49]. In this analysis, a Raman time constant of 2.4 fs was extracted by fitting the data. This time

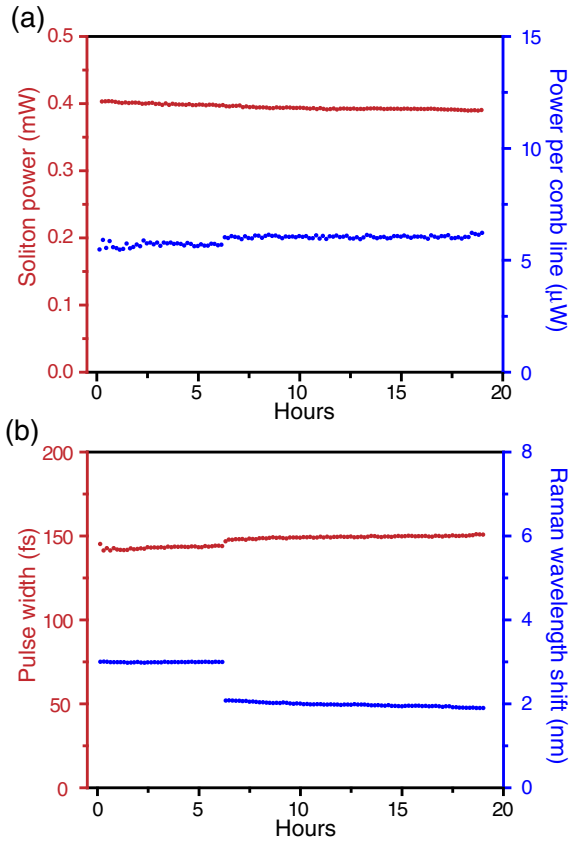


**Fig. 4.** Continuous soliton measurement over 19 h. (a) The soliton power and central comb line power are plotted versus time in hours. The soliton power experiences a slow drift to lower values, which is attributed to a slow variation in either the power set point of the electronic control or in the detected power (perhaps due to temperature drift). The central comb line power is approximately constant over the measured period, with the exception of a small step increase around 6 h. This could be associated with anything that increases the resonator coupling efficiency, decreases the resonator  $Q$ , or both. Since the resonator is taper coupled, any kind of mechanical shock could introduce such a step change in these quantities. (b) Pulse width and Raman self-shift (defined as the wavelength center of the soliton spectrum less the pump wavelength) are plotted versus time in hours. A step in these quantities is recorded at the identical moment to that recorded for the central comb line power. It is interesting to note that because the soliton power is feedback controlled, from Eq. (2), a step increase (decrease) in coupling  $\eta$  ( $Q$ ) would be accompanied by a compensating decrease (increase) in pump detuning. From Eq. (3), this feedback-controlled step in detuning would cause an increase in the soliton pulse width (and decrease in the Raman shift), as observed in the recorded data of panel b. Finally, the operation of the soliton comb proceeded for an additional 5 h beyond the record presented in this figure. During the additional 5 h, other measurements were performed that required disabling the data recording.

constant closely agrees with a value of 3 fs measured for a silica optical fiber [50]. The contribution of the Raman terms is both predicted and measured to be stronger for shorter pulses (or equivalently larger  $\delta\omega$ ). These observations are also consistent with the modeling, which shows modifications to soliton efficiency as a result of the Raman process [49].

It is interesting that the predicted soliton power and power per line do not require a Raman correction [see Fig. 3(a)]. The Raman correction primarily influences the temporal phase of the soliton pulse and not the amplitude [38]. It would therefore be expected to alter the existence condition, which is associated with the

phase of the soliton field, and not the power per line or overall comb power.

All of the soliton spectra observed in this work were red shifted relative to the pump wavelength. Raman interaction with dissipative Kerr solitons has recently been shown to cause such self-shifting of the spectrum [38,51,52]. The effect has been observed in silicon nitride resonators [38]. Like the correction to the minimum power described above, this shift is stronger for shorter pulses and larger detuning frequencies. Shifted soliton spectra can be produced by several mechanisms [53] besides Raman, including soliton recoil caused by dispersive wave generation [26]. There was no evidence of dispersive wave generation at shorter wavelengths in this work. Consistent with other reports [38], the Raman-augmented LLE simulation explains the soliton spectral shift observed here [see orange and green curves in Fig. 3(b)].

Control of the pump-resonator detuning frequency enables stable operation near an optimal pumping efficiency limit. Defining the efficiency [49] as the soliton power divided by the minimum pump power for soliton existence gives the following simple expression:

$$\Gamma \equiv \pi \eta^2 D_1 \tau. \quad (7)$$

A comparison of this prediction with the measurement is provided in Fig. 3(c) ( $\eta = 0.29$  in this measurement). A deviation between the simple formula [Eq. (7)] and the data at small pulse widths occurs on account of the Raman effects and has been corrected in the figure (small dashed blue line) using the Raman-augmented LLE result.

## 6. DISCUSSION

Reduced soliton repetition rates ( $D_1/2\pi$ ) are accompanied by an increased mode volume, and therefore require greater pumping

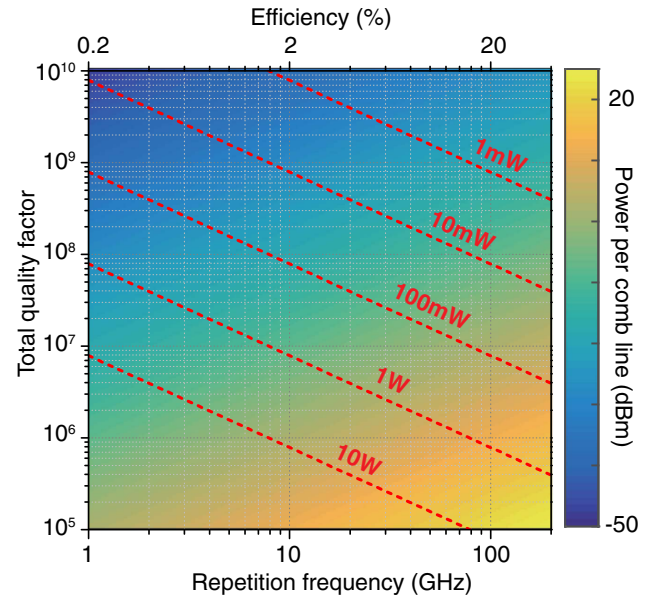


**Fig. 5.** Required pumping power and maximum power per comb line. Linear contours give the minimum pump power required for existence of 200 fs solitons assuming the silica resonator of this work with the indicated  $Q$ -factor and repetition frequency (note that scales change for other material systems). These are derived using Eq. (6). Coloration indicates the maximum power per comb line given by Eq. (5). The upper horizontal axis is the efficiency found using Eq. (7). This axis does not depend on the material.  $\eta = 0.7$  is assumed in making the plot.



powers to maintain the nonlinear coupling of the modes, as is evident in Eq. (1) for a parametric threshold [19,23]. The compensating effect of  $Q$  on this dependence is apparent in Eq. (1) and also in the expression for the minimum pump power for soliton existence [Eq. (6)]. For a fixed pulse duration  $\tau$  (equivalently fixed comb bandwidth), the required input power is inversely proportional to repetition rate and  $Q$ -factor (equal to finesse  $\times$  optical frequency). Figure 5 shows the contours of constant existence power versus the  $Q$ -factor and repetition frequency [Eq. (6)]. The plot assumes material parameters for the silica and a 200 fs soliton pulse width. The contour powers represent an absolute minimum. In practice, a pumping level higher than this value is required for stable operation. However, as shown in the previous sections, it is possible to operate close to this minimum using the detuning lock approach. The maximum power per comb line varies linearly with the repetition frequency and inversely with the cavity  $Q$ -factor and is represented by the color shading in Fig. 5. Also, the efficiency is shown on the upper axis assuming a coupling efficiency  $\eta = 0.7$  corresponding to a slightly over-coupled condition. The theoretical efficiency limit is actually  $2\times$  higher than shown on this scale, and could be achieved by using a resonator that is highly over coupled.

Cavity dispersion control methods have been demonstrated using a modification to the standard wedge resonator process [54]. These same methods might be applied to control dispersive wave generation within the resonator to achieve the direct generation of a broader comb. The ability to generate solitons on a chip at rates commensurate with detectors and low-noise electronics is an essential step in the ultimate goal of a fully integrated comb system. Besides soliton generation, the silica wedge resonator platform has been used to generate ultra-narrow linewidth laser sources [55,56] and high- $Q$  reference cavities [57], and can be used for continuum generation [58]. These elements are required in both self-referenced combs as well their application to clocks, high-stability microwave sources, and optical synthesizers. The results presented here therefore add to this suite of technologically compatible devices.

**Funding.** Defense Advanced Research Projects Agency (DARPA) (W31P4Q-14-1-0001, W911NF-14-1-0284); National Aeronautics and Space Administration (NASA) (KJV.JPLNASA-1-JPL.1459106); Kavli Nanoscience Institute; Institute for Quantum Information and Matter, National Science Foundation (NSF) Physics Frontiers Center (PHY-1125565); Gordon and Betty Moore Foundation.

**Acknowledgment.** The authors thank Tobias Kippenberg and Victor Brasch at EPFL and also Michael Gorodetsky at Moscow State University for the helpful discussions and comments on this paper. The authors gratefully acknowledge the Defense Advanced Research Projects Agency (DARPA) under the QuASAR program (W911NF-14-1-0284) and PULSE programs (W31P4Q-14-1-0001), the National Aeronautics and Space Administration (NASA) (KJV.JPLNASA-1-JPL.1459106), the Kavli Nanoscience Institute, and the Institute for Quantum Information and Matter, a National Science Foundation (NSF) Physics Frontiers Center (PHY-1125565) with support of the Gordon and Betty Moore Foundation.

†These authors contributed equally to this work.

## REFERENCES

1. D. J. Jones, S. A. Diddams, J. K. Ranka, A. Stentz, R. S. Windeler, J. L. Hall, and S. T. Cundiff, "Carrier-envelope phase control of femtosecond mode-locked lasers and direct optical frequency synthesis," *Science* **288**, 635–639 (2000).
2. R. Holzwarth, Th. Udem, T. W. Hänsch, J. Knight, W. Wadsworth, and P. St. J. Russell, "Optical frequency synthesizer for precision spectroscopy," *Phys. Rev. Lett.* **85**, 2264–2267 (2000).
3. S. Diddams, T. Udem, J. Bergquist, E. Curtis, R. Drullinger, L. Hollberg, W. Itano, W. Lee, C. Oates, K. Vogel, and D. Wineland, "An optical clock based on a single trapped  $^{199}\text{Hg}^+$  ion," *Science* **293**, 825–828 (2001).
4. T. Udem, R. Holzwarth, and T. W. Hänsch, "Optical frequency metrology," *Nature* **416**, 233–237 (2002).
5. S. Diddams, J. Bergquist, S. Jefferts, and C. Oates, "Standards of time and frequency at the outset of the 21st century," *Science* **306**, 1318–1324 (2004).
6. N. R. Newbury, "Searching for applications with a fine-tooth comb," *Nat. Photonics* **5**, 186–188 (2011).
7. T. Steinmetz, T. Wilken, C. Araujo-Hauck, R. Holzwarth, T. W. Hänsch, L. Pasquini, A. Manescau, S. D'Odorico, M. T. Murphy, T. Kentscher, W. Schmidt, and T. Udem, "Laser frequency combs for astronomical observations," *Science* **321**, 1335–1337 (2008).
8. C.-H. Li, A. J. Benedick, P. Fendel, A. G. Glenday, F. X. Kärtner, D. F. Phillips, D. Sasselov, A. Szentgyorgyi, and R. L. Walsworth, "A laser frequency comb that enables radial velocity measurements with a precision of  $1\text{ cm s}^{-1}$ ," *Nature* **452**, 610–612 (2008).
9. T. Fortier, M. Kirchner, F. Quinlan, J. Taylor, J. Bergquist, T. Rosenband, N. Lemke, A. Ludlow, Y. Jiang, C. Oates, and S. Diddams, "Generation of ultrastable microwaves via optical frequency division," *Nat. Photonics* **5**, 425–429 (2011).
10. P. Del'Haye, A. Schliesser, O. Arcizet, T. Wilken, R. Holzwarth, and T. Kippenberg, "Optical frequency comb generation from a monolithic microresonator," *Nature* **450**, 1214–1217 (2007).
11. T. J. Kippenberg, R. Holzwarth, and S. Diddams, "Microresonator-based optical frequency combs," *Science* **332**, 555–559 (2011).
12. A. A. Savchenko, A. B. Matsko, V. S. Ilchenko, I. Solomatine, D. Seidel, and L. Maleki, "Tunable optical frequency comb with a crystalline whispering gallery mode resonator," *Phys. Rev. Lett.* **101**, 093902 (2008).
13. I. S. Grudinin, N. Yu, and L. Maleki, "Generation of optical frequency combs with a  $\text{CaF}_2$  resonator," *Opt. Lett.* **34**, 878–880 (2009).
14. S. B. Papp and S. A. Diddams, "Spectral and temporal characterization of a fused-quartz-microresonator optical frequency comb," *Phys. Rev. A* **84**, 053833 (2011).
15. B. Hausmann, I. Bulu, V. Venkataraman, P. Deotare, and M. Lončar, "Diamond nonlinear photonics," *Nat. Photonics* **8**, 369–374 (2014).
16. J. S. Levy, A. Gondarenko, M. A. Foster, A. C. Turner-Foster, A. L. Gaeta, and M. Lipson, "CMOS-compatible multiple-wavelength oscillator for on-chip optical interconnects," *Nat. Photonics* **4**, 37–40 (2010).
17. L. Razzari, D. Duchesne, M. Ferrera, R. Morandotti, S. Chu, B. Little, and D. Moss, "CMOS-compatible integrated optical hyper-parametric oscillator," *Nat. Photonics* **4**, 41–45 (2010).
18. F. Ferdous, H. Miao, D. E. Leaird, K. Srinivasan, J. Wang, L. Chen, L. T. Varghese, and A. M. Weiner, "Spectral line-by-line pulse shaping of on-chip microresonator frequency combs," *Nat. Photonics* **5**, 770–776 (2011).
19. J. Li, H. Lee, T. Chen, and K. J. Vahala, "Low-pump-power, low-phase-noise, and microwave to millimeter-wave repetition rate operation in microcombs," *Phys. Rev. Lett.* **109**, 233901 (2012).
20. H. Jung, C. Xiong, K. Y. Fong, X. Zhang, and H. X. Tang, "Optical frequency comb generation from aluminum nitride microring resonator," *Opt. Lett.* **38**, 2810–2813 (2013).
21. S. B. Papp, K. Beha, P. Del'Haye, F. Quinlan, H. Lee, K. J. Vahala, and S. A. Diddams, "Microresonator frequency comb optical clock," *Optica* **1**, 10–14 (2014).
22. J. Pfeifle, V. Brasch, M. Laueremann, Y. Yu, D. Wegner, T. Herr, K. Hartinger, P. Schindler, J. Li, D. Hillerkuss, R. Schmogrow, C. Weimann, R. Holzwarth, W. Freude, J. Leuthold, T. Kippenberg, and C. Koos, "Coherent terabit communications with microresonator Kerr frequency combs," *Nat. Photonics* **8**, 375–380 (2014).
23. T. Kippenberg, S. Spillane, and K. Vahala, "Kerr-nonlinear optical parametric oscillation in an ultrahigh-Q toroid microcavity," *Phys. Rev. Lett.* **93**, 083904 (2004).

24. A. A. Savchenkov, A. B. Matsko, D. Strekalov, M. Mohageg, V. S. Ilchenko, and L. Maleki, "Low threshold optical oscillations in a whispering gallery mode  $\text{CaF}_2$  resonator," *Phys. Rev. Lett.* **93**, 243905 (2004).
25. T. Herr, V. Brasch, J. Jost, C. Wang, N. Kondratiev, M. Gorodetsky, and T. Kippenberg, "Temporal solitons in optical microresonators," *Nat. Photonics* **8**, 145–152 (2014).
26. V. Brasch, T. Herr, M. Geiselmann, G. Lihachev, M. H. P. Pfeiffer, M. L. Gorodetsky, and T. J. Kippenberg, "Photonic chip based optical frequency comb using soliton induced Cherenkov radiation," *ArXiv*: 1410.8598 (2014).
27. T. Herr, K. Hartinger, J. Riemensberger, C. Wang, E. Gavartin, R. Holzwarth, M. Gorodetsky, and T. Kippenberg, "Universal formation dynamics and noise of Kerr-frequency combs in microresonators," *Nat. Photonics* **6**, 480–487 (2012).
28. P. Del'Haye, K. Beha, S. B. Papp, and S. A. Diddams, "Self-injection locking and phase-locked states in microresonator-based optical frequency combs," *Phys. Rev. Lett.* **112**, 043905 (2014).
29. P. Del'Haye, A. Coillet, W. Loh, K. Beha, S. B. Papp, and S. A. Diddams, "Phase steps and resonator detuning measurements in microresonator frequency combs," *Nat. Commun.* **6**, 5668 (2015).
30. S. B. Papp, P. Del'Haye, and S. A. Diddams, "Parametric seeding of a microresonator optical frequency comb," *Opt. Express* **21**, 17615–17624 (2013).
31. K. Saha, Y. Okawachi, B. Shim, J. S. Levy, R. Salem, A. R. Johnson, M. A. Foster, M. R. Lamont, M. Lipson, and A. L. Gaeta, "Modelocking and femtosecond pulse generation in chip-based frequency combs," *Opt. Express* **21**, 1335–1343 (2013).
32. S. Wang, H. Guo, X. Bai, and X. Zeng, "Broadband Kerr frequency combs and intracavity soliton dynamics influenced by high-order cavity dispersion," *Opt. Lett.* **39**, 2880–2883 (2014).
33. A. Ankiewicz and N. Akhmediev, *Dissipative Solitons: From Optics to Biology and Medicine* (Springer, 2008).
34. F. Leo, S. Coen, P. Kockaert, S.-P. Gorza, P. Emplit, and M. Haelterman, "Temporal cavity solitons in one-dimensional Kerr media as bits in an all-optical buffer," *Nat. Photonics* **4**, 471–476 (2010).
35. I. S. Grudinin and N. Yu, "Towards efficient octave-spanning comb with micro-structured crystalline resonator," *Proc. SPIE* **9343**, 93430F (2015).
36. W. Liang, D. Eliyahu, V. Ilchenko, A. Savchenkov, A. Matsko, D. Seidel, and L. Maleki, "High spectral purity Kerr frequency comb radio frequency photonic oscillator," *Nat. Commun.* **6**, 7957 (2015).
37. J. D. Jost, T. Herr, C. Lecaplain, V. Brasch, M. H. P. Pfeiffer, and T. J. Kippenberg, "Counting the cycles of light using a self-referenced optical microresonator," *Optica* **2**, 706–711 (2015).
38. M. Karpov, H. Guo, A. Kordts, V. Brasch, M. Pfeiffer, M. Zervas, M. Geiselmann, and T. J. Kippenberg, "Raman induced soliton self-frequency shift in microresonator Kerr frequency combs," *arXiv preprint arXiv:1506.08767* (2015).
39. H. Lee, T. Chen, J. Li, K. Y. Yang, S. Jeon, O. Painter, and K. J. Vahala, "Chemically etched ultrahigh-Q wedge-resonator on a silicon chip," *Nat. Photonics* **6**, 369–373 (2012).
40. T. Herr, V. Brasch, J. Jost, I. Mirgorodskiy, G. Lihachev, M. Gorodetsky, and T. Kippenberg, "Mode spectrum and temporal soliton formation in optical microresonators," *Phys. Rev. Lett.* **113**, 123901 (2014).
41. J. Li, H. Lee, K. Y. Yang, and K. J. Vahala, "Sideband spectroscopy and dispersion measurement in microcavities," *Opt. Express* **20**, 26337–26344 (2012).
42. T. Carmon, L. Yang, and K. Vahala, "Dynamical thermal behavior and thermal self-stability of microcavities," *Opt. Express* **12**, 4742–4750 (2004).
43. S. Wabnitz, "Suppression of interactions in a phase-locked soliton optical memory," *Opt. Lett.* **18**, 601–603 (1993).
44. A. B. Matsko and L. Maleki, "On timing jitter of mode locked Kerr frequency combs," *Opt. Express* **21**, 28862–28876 (2013).
45. L. A. Lugiato and R. Lefever, "Spatial dissipative structures in passive optical systems," *Phys. Rev. Lett.* **58**, 2209–2211 (1987).
46. A. Matsko, A. Savchenkov, W. Liang, V. Ilchenko, D. Seidel, and L. Maleki, "Mode-locked Kerr frequency combs," *Opt. Lett.* **36**, 2845–2847 (2011).
47. Y. K. Chembo and C. R. Menyuk, "Spatiotemporal Lugiato-Lefever formalism for Kerr-comb generation in whispering-gallery-mode resonators," *Phys. Rev. A* **87**, 053852 (2013).
48. G. P. Agrawal, *Nonlinear Fiber Optics* (Academic, 2007).
49. C. Bao, L. Zhang, A. Matsko, Y. Yan, Z. Zhao, G. Xie, A. M. Agarwal, L. C. Kimerling, J. Michel, L. Maleki, and A. E. Willner, "Nonlinear conversion efficiency in Kerr frequency comb generation," *Opt. Lett.* **39**, 6126–6129 (2014).
50. A. Atieh, P. Myslinski, J. Chrostowski, and P. Galko, "Measuring the Raman time constant ( $t_r$ ) for soliton pulses in standard single-mode fiber," *J. Lightwave Technol.* **17**, 216–221 (1999).
51. F. M. Mitschke and L. F. Mollenauer, "Discovery of the soliton self-frequency shift," *Opt. Lett.* **11**, 659–661 (1986).
52. J. P. Gordon, "Theory of the soliton self-frequency shift," *Opt. Lett.* **11**, 662–664 (1986).
53. L. Zhang, Q. Lin, L. C. Kimerling, and J. Michel, "Self-frequency shift of cavity soliton in Kerr frequency comb," *arXiv preprint arXiv:1404.1137* (2014).
54. K. Y. Yang, K. Beha, D. C. Cole, X. Yi, P. Del'Haye, H. Lee, J. Li, D. Y. Oh, S. A. Diddams, S. B. Papp, and K. J. Vahala, "Broadband dispersion engineered microresonator on-a-chip," *arXiv preprint arXiv:1506.07157* (2015).
55. J. Li, H. Lee, T. Chen, and K. J. Vahala, "Characterization of a high coherence, Brillouin microcavity laser on silicon," *Opt. Express* **20**, 20170–20180 (2012).
56. W. Loh, A. A. Green, F. N. Baynes, D. C. Cole, F. J. Quinlan, H. Lee, K. J. Vahala, S. B. Papp, and S. A. Diddams, "Dual-microcavity narrow-line-width Brillouin laser," *Optica* **2**, 225–232 (2015).
57. H. Lee, M.-G. Suh, T. Chen, J. Li, S. A. Diddams, and K. J. Vahala, "Spiral resonators for on-chip laser frequency stabilization," *Nat. Commun.* **4**, 2468 (2013).
58. D. Y. Oh, D. Sell, H. Lee, K. Y. Yang, S. A. Diddams, and K. J. Vahala, "Supercontinuum generation in an on-chip silica waveguide," *Opt. Lett.* **39**, 1046–1048 (2014).